Identification of the Active-layer Structures for Acidic Oxygen Evolution from 9R-BaIrO₃ Electrocatalyst with Enhanced Iridium Mass Activity

Na Li^{1†}, Liang Cai^{1,2*†}, Chao Wang¹, Yue Lin³, Jinzhen Huang^{2,4}, Hongyuan Sheng², Haibin Pan¹, Wei Zhang¹, Qianqian Ji¹, Hengli Duan¹, Wei Hu¹, Wenhua Zhang¹, Fengchun Hu¹, Hao Tan¹, Zhihu Sun¹, Bo Song⁴, Song Jin^{2*}, Wensheng Yan^{1*}

†These authors contributed equally to this work.

*Corresponding authors: E-mail: lcai@mail.ustc.edu.cn; ywsh2000@ustc.edu.cn; jin@chem.wisc.edu

Abstract

Iridium-based perovskites show promising catalytic activity for oxygen evolution reaction (OER) in acid media, but the iridium mass activity remains low and the active-layer structures have not been identified. Here we report highly active 1-nm IrO_x particles anchored on 9R-BaIrO₃ (IrO_x/9R-BaIrO₃) that are directly synthesized by solution calcination followed by strong acid treatment for the first time. The developed IrO_x/9R-BaIrO₃ catalyst delivers a high iridium mass activity (168 A g_{Ir}^{-1}), about 16 times higher than that of the benchmark acidic OER electrocatalyst IrO₂ (10 A g_{Ir}^{-1}), and only requires a low overpotential of 230 mV to reach a catalytic current density of 10 mA cm⁻ ²_{geo.} Careful scanning transmission electron microscopy, synchrotron radiation-based X-ray absorption spectroscopy, and X-ray photoelectron spectroscopy analyses reveal that, during the electrocatalytic process, the initial 1-nm IrO_x nanoparticles/9R-BaIrO₃ evolve into amorphous Ir⁴⁺O_xH_y/IrO₆ octahedrons and then to amorphous Ir⁵⁺O_x/IrO₆ octahedrons on the surface. Such high relative content of amorphous Ir⁵⁺O_x species derived from trimers of face-sharing IrO₆ octahedrons in 9R-BaIrO₃ and the enhanced metallic conductivity of the Ir⁵⁺O_x/9R-BaIrO₃ catalyst are responsible for the excellent acidic OER activity. Our results provide new insights into the surface active-layer structure evolution in perovskite electrocatalysts and demonstrate new approaches for engineering highly active acidic OER nanocatalysts.

¹National Synchrotron Radiation Laboratory, University of Science and Technology of China, Hefei, Anhui 230029, PR China

²Department of Chemistry, University of Wisconsin—Madison, Madison, Wisconsin 53706, United States

³Hefei National Laboratory for Physical Sciences at the Microscale, University of Science and Technology of China, Hefei, Anhui 230029, PR China

⁴Center for Composite Materials and Structures, Harbin Institute of Technology, Harbin 150001, PR China

Keywords: acidic OER electrocatalysis, Iridium-based perovskites, IrO_x , active-layer structures, iridium mass activity, surface structure evolution

Introduction

Electrochemical water-splitting plays a critical role in clean and renewable energy technologies, but the sluggish oxygen evolution reaction (OER) at the anode largely limits the performance and industrial applications of electrochemical water splitting.¹⁻³ A large number of OER electrocatalysts have been investigated to exhibit activity and stability in alkaline electrolyte.⁴⁻¹¹ In order to overcome the disadvantages of conventional alkaline electrolyzers, proton exchange membrane (PEM)-based water electrolyzers have been developed as a more promising technology.¹² At present, considering both activity and stability,¹³ iridium oxides (IrO₂¹⁴ or IrO_x¹⁵) are the viable OER catalysts that show good durability in harsh acidic media. However, the high-cost and scarcity of the precious iridium oxide catalyst greatly hinder the practical applications of PEM water electrolysis.¹²⁻¹³ Various approaches have been employed to develop low-iridium loading but efficient OER electrocatalysts to maximize the iridium mass activity in iridium-based catalysts.¹⁶⁻¹⁹ To date, only a few electrocatalysts have been reported to exhibit efficient yet stable OER catalysis in acidic media.^{3, 9, 20-22} Therefore, the development of new iridium-based OER electrocatalysts with higher iridium mass activity and long-term electrochemical stability in acidic media is highly desirable.

Toward this goal, iridium-based perovskite oxides²³⁻²⁸ have been recently investigated for acidic OER electrocatalysis. For example, 3C-SrIrO₃ thin films deposited on SrTiO₃ substrates by pulsed laser deposition (PLD) exhibited enhanced OER catalytic activity and stability in acidic media after a 2-hour electrochemical activation process.²³ Density functional theory (DFT) calculations suggested that IrO3 or anatase IrO2, which were formed on the 3C-SrIrO3 surface due to Sr dissolution during electrocatalytic process, may be responsible for the catalytic activity. However, the evolved active-layer structures were not verified in experiment. 6H-SrIrO₃ was also reported to be an efficient electrocatalyst under acidic conditions, and theoretical calculations proposed that the face-sharing IrO₆ octahedral dimers in 6H-SrIrO₃ may be responsible for the excellent catalytic activity.²⁴ A detailed study of 6H-SrIrO₃ catalyst synthesized by conventional solid-state reaction (CSSR)²⁵ demonstrated that the electrochemical activity and stability are totally different from the catalyst synthesized by wet-chemical method.²⁴ Similarly, it was observed that the electrocatalytic properties of IrO₂ vary greatly depending on their different synthesis routes due to the different surface structures.^{20, 29} The surface structures of the iridiumbased perovskites synthesized by PLD or CSSR methods are not active by themselves, ^{23, 25-26} and the electrochemical stabilities for some of these catalysts are poor, ²⁵⁻²⁶ especially, the iridium mass activities for some of these catalysts are low. ^{23,26} All of these limit the applications of such iridiumbased perovskite electrocatalysts. Due to the limitations of characterization techniques, the real active-layer structures of the nanoscale oxides electrochemically formed on the surface of Ir-based

perovskites have remained poorly understood and controversial.²³⁻²⁵ Achieving highly active catalytic structures anchored on perovskite electrocatalysts with higher iridium mass activity and systematically unravelling the surface active-layer nanostructure evolution in Ir-based perovskite electrocatalysts remain key challenges.

Here we report the 1-nm IrO_x particles uniformly anchored on 9R-BaIrO₃ (IrO_x/9R-BaIrO₃) as an outstanding electrocatalyst for the acidic OER. This catalyst is conveniently formed by a new direct synthesis of 9R-BaIrO₃ via solution calcination followed by a strong acid treatment. The resulting IrO_x/9R-BaIrO₃ catalyst exhibits the highest iridium mass activity (168 A g_{Ir}⁻¹) among the reported iridium-based perovskite electrocatalysts for the acidic OER, which is about 16 times higher than the that of IrO₂ (10 A g_{Ir}⁻¹), the benchmark electrocatalyst in acidic electrolyte. This catalyst requires only a low overpotential of 230 mV to achieve a current density of 10 mA cm⁻²geo and displays good electrochemical stability. Careful characterization using lattice-resolved scanning transmission electron microscopy (STEM), synchrotron radiation-based X-ray absorption spectroscopy (XAS) and X-ray photoelectron spectroscopy (XPS), systematically reveal the surface active-layer nanostructure evolution in IrO_x/9R-BaIrO₃. The abundance of higher-valence amorphous iridium oxide species formed from the 1-nm IrO_x particles on the surface of 9R-BaIrO₃ and the enhanced metallic conductivity of IrO_x/9R-BaIrO₃ can account for the excellent acidic OER activity of IrO_x/9R-BaIrO₃ catalyst.

Results and Discussion

We developed a new synthesis method via solution calcination to synthesize 9R-BaIrO₃ and subsequently used a strong acid treatment to leach some Ba atoms and form the 1-nm IrO_x particles uniformly anchored on the surface of 9R-BaIrO₃ (IrO_x/9R-BaIrO₃) (see Methods and Figure S1-3 for details). At ambient pressure, BaIrO₃ crystalizes in the 9R polytype with monoclinic distortion (*C*2/*m* space group),³⁰ which contains trimers of face-sharing IrO₆ octahedrons that are linked by their vertices to form columns along the *c* axis (Figure 1a). To identify the initial active-layer structures on the surface of 9R-BaIrO₃, we introduce 1 M hydrochloric acid (HCl) to leach the Ba metal ions and reconstruct the surface structures, a hypothesized illustration of which is shown in Figure 1b. X-ray diffraction (XRD) pattern of this post-acid treatment sample (Figure 1c) shows that the strongest set of diffraction peaks are consistent with those of 9R-phase BaIrO₃ (JCPDS PDF#44-0021). The three weak diffraction peaks (28.9°, 34.4° and 58.6°) in Figure 1c could be matched with IrO_x, based on the comparison with theoretically predicted PXRD of such phase from the Materials Project (ID: 1022963). Scanning electron microscopy (SEM) image (Figure 1d) reveals nano-sized, plate-like crystals. Energy dispersive X-ray (EDX) mapping images (Figure S4) reveal that Ba and Ir elements are uniformly distributed in these plates.

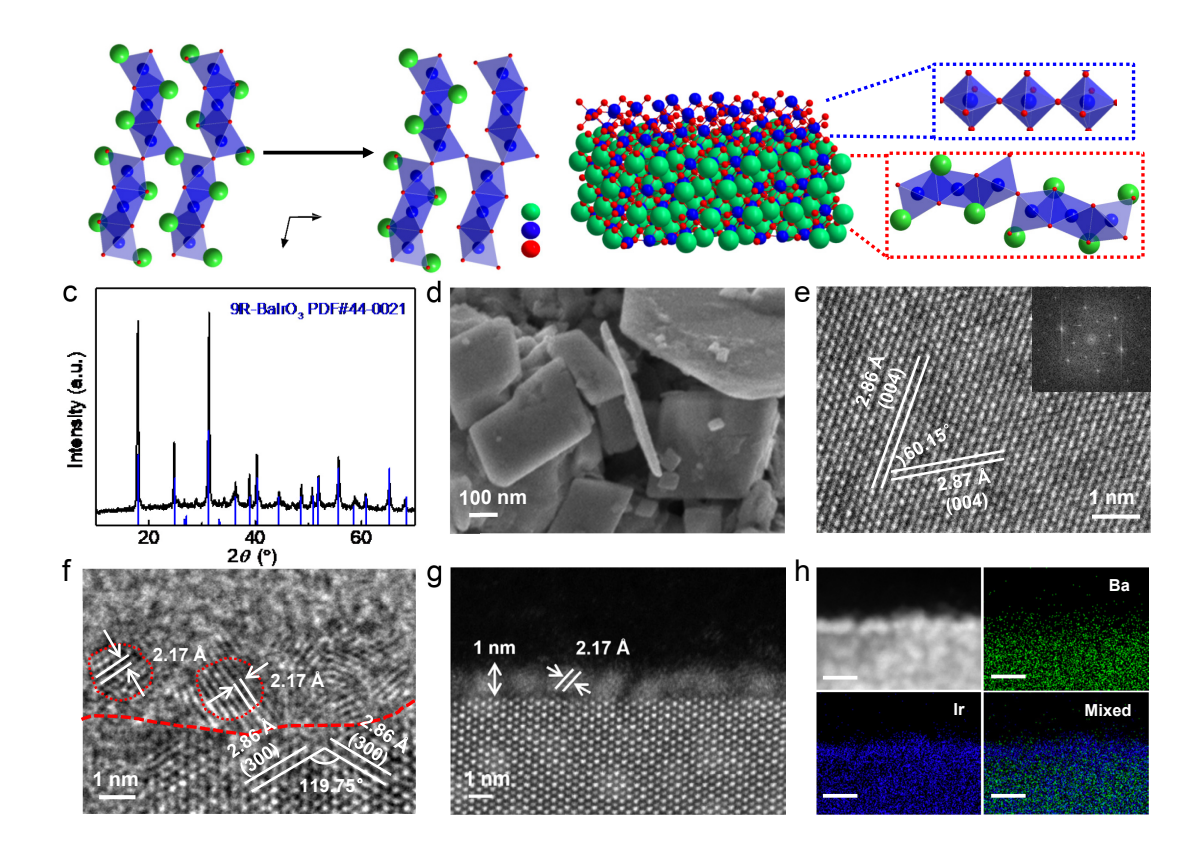


Figure 1. Structure characterizations of IrO_x/9R-BaIrO₃ catalyst. (a) A schematic illustrating the changes in the 9R-BaIrO₃ crystal structure (left) after the HCl treatment, which shows the trimers of face-sharing IrO₆ octahedrons (right) are formed after Ba leaching. (Ba, green ball; Ir, blue ball; O, red ball). (b) Schematic representation of the hypothesized surface layer of 9R-BaIrO₃ after Ba leaching and surface reconstructions. (c) XRD pattern of the IrO_x/9R-BaIrO₃ sample. (d) SEM image of IrO_x/9R-BaIrO₃ nanoplates after acid treatment. (e) HRTEM image shows the representative lattice fringes of ~0.286 nm corresponding to the (004) plane of 9R-BaIrO₃ and the corresponding FFT image (inset). (f) HRTEM image of the surface of IrO_x/9R-BaIrO₃ shows nanoparticles with very different lattice spacing of 0.217 nm, indicating the nanoparticles are not IrO₂. (g) HAADF-STEM image revealing 1 nm nanoparticles uniformly anchored on the surface of 9R-BaIrO₃. (h) STEM-EDX mapping images show the 1 nm nanoparticles are Ir-rich (scale bar, 5 nm).

High-resolution transmission electron microscopy (HRTEM) image (Figure 1e) shows the representative lattice fringes of ~0.286 nm corresponding to the (004) plane of 9R-BaIrO₃. The corresponding fast Fourier transform (FFT) image (inset in Figure 1e) further confirms the crystallinity and crystal structure of the 9R-BaIrO₃ sample. Figure 1f shows the surface structures of 9R-BaIrO₃ crystals and reveals a rather different lattice spacing of 0.217 nm, which indicates that the nanoparticles are not IrO₂ (see Table S1, hereafter called IrO_x). High-angle annular dark field (HAADF) STEM image (Figure 1g) further reveals nanoparticles uniformly anchored on the

surface of the 9R-BaIrO₃ plates. STEM-EDX mapping images (Figure 1h) reveal that the nanoparticles are Ir-rich. These structure characterizations confirm that during the acid treatment process the trimers of face-sharing IrO₆ octahedrons on the surface of 9R-BaIrO₃ are transformed into IrO_x nanoparticles, which were believed to be highly active surface layers for acidic OER.^{23,} 31-32

The electrochemical OER performance of the IrO_x/9R-BaIrO₃ catalyst was evaluated in acidic solution (O2-saturated 0.5 M H2SO4), together with commercial IrO2 and as-synthesized 6H-SrIrO3 catalyst²⁴ as comparisons. The full details of the structural characterization of the 6H-SrIrO₃ sample are shown in Figure S5-7. As shown in Figure 2a, commercial IrO2 shows a large overpotential of 330 mV to reach a catalytic current density of 10 mA cm⁻²geo, which is in line with previous reports. 14, 33 The IrO_x/9R-BaIrO₃ electrocatalyst only requires a low overpotential of 230 mV to reach the current density of 10 mA cm⁻²_{geo}, which is substantially reduced by 100 mV and 70 mV from those by the commercial IrO₂ and as-synthesized 6H-SrIrO₃ (300 mV), respectively. The reported overpotentials for leached 3C-SrIrO₃²³ are also shown as horizontal bars as comparison. The outstanding OER activity of IrO_x/9R-BaIrO₃ is also reflected by the smallest Tafel slope of 80 mV/dec (Figure 2b) compared to that of IrO₂ (159 mV/dec) and 6H-SrIrO₃ (122 mV/dec), indicating the OER kinetic over IrOx/9R-BaIrO3 is significantly accelerated. This is further confirmed by the electrochemical impedance spectroscopy (EIS) measurements of these three catalysts tested under the same conditions (Figure 2c). Nyquist plots show that the charge transfer resistance (Rct) for IrOx/9R-BaIrO3 is as low as 20 Ohm, one order of magnitude smaller than that of 6H-SrIrO₃ and IrO₂ (>400 Ohm).

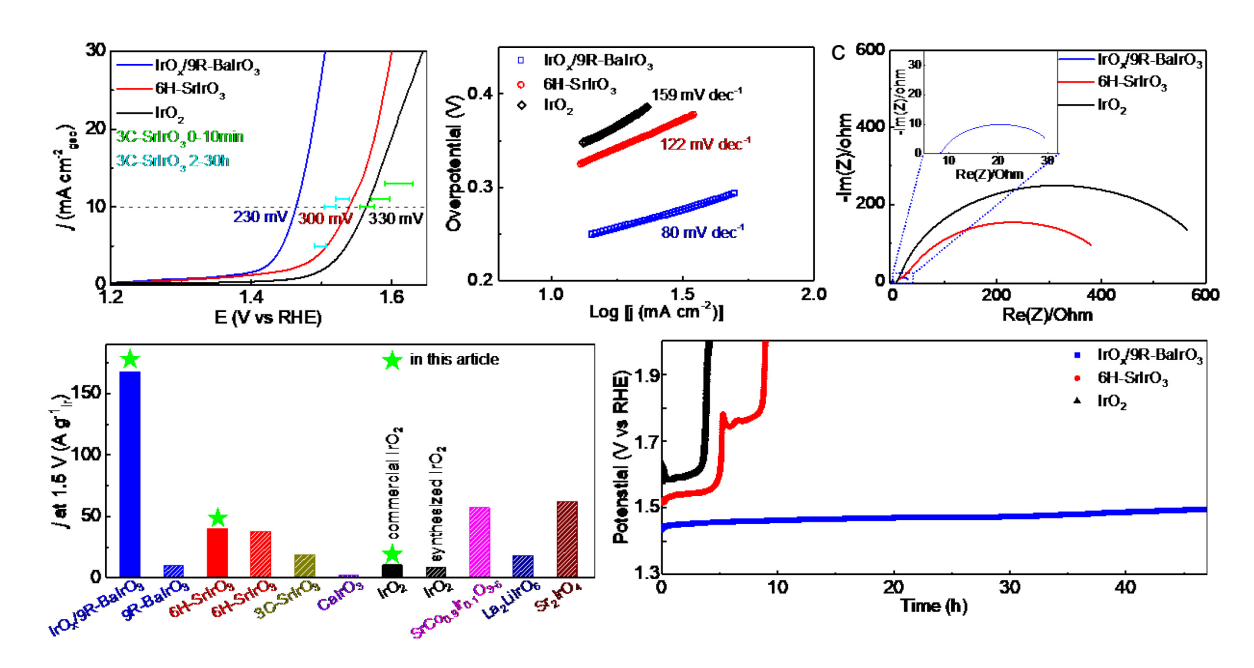


Figure 2. Electrochemical OER performance of IrO_x/9R-BaIrO₃ in comparison with other catalysts in acidic solution. (a) Polarization curves of IrO_x/9R-BaIrO₃, commercial IrO₂ and as-

synthesized 6H-SrIrO₃ measured in O₂-saturated 0.5 M H₂SO₄. The specific OER overpotentials at 10 mA cm⁻²_{geo} of 3C-SrIrO₃ after the specific leaching times in 0.5 M H₂SO₄ from the reference²³ are shown as horizontal bars. (b) The corresponding Tafel plots, and (c) the EIS Nyquist plots of the same samples measured at 1.53 V vs. RHE. Glassy carbon electrode was used as the catalyst support for electrochemical OER performance shown in (a), (b) and (c). (d) Comparison of the iridium mass activity at 1.5 V vs. RHE for IrO_x/9R-BaIrO₃ and some recently reported iridium-based perovskite OER catalysts in acid media. (e) Chronopotentiometric measurements of IrO_x/9R-BaIrO₃, commercial IrO₂ and as-synthesized 6H-SrIrO₃ at 10 mA cm⁻²_{geo}. Carbon paper was used as the catalyst support for chronopotentiometric measurement in (e).

The iridium mass activity of the electrocatalysts for acidic OER is important. In Figure 2d, we compare the iridium mass activity of the IrO_x/9R-BaIrO₃ catalyst, expressed as the current per unit mass of Ir (A g⁻¹) at the potential of 1.5 V (see definition in Materials and Methods), with the state-of-the-art iridium-based perovskite electrocatalysts reported up to date. ^{14, 23-26, 33-36} The iridium mass activity for commercial IrO₂ (10 A g_{Ir}⁻¹) and as-synthesized 6H-SrIrO₃ (40 A g_{Ir}⁻¹) are calculated from the results above and labeled with green stars, which are consistent with recent reports. ^{14, 24} The mass activity of IrO_x/9R-BaIrO₃ (168 A g_{Ir}⁻¹) is 16 times higher than that of commercial IrO₂ and 4 times higher than that of 6H-SrIrO₃. The IrO_x/9R-BaIrO₃ catalyst exhibits the highest iridium mass activity at 1.5 V versus reversible hydrogen electrode (RHE) for acidic OER among various iridium-based perovskite electrocatalysts recently reported.

It is worth noting that the excellent electrocatalytic performance of IrO_x/9R-BaIrO₃ does not correlate with its electrochemically active surface areas (ECSA), which could be estimated by the electrochemical double-layer capacitance ($C_{\rm dl}$). As shown in Figure S8, the $C_{\rm dl}$ of IrO_x/9R-BaIrO₃, 6H-SrIrO₃ and IrO₂ are estimated to be 1.59 mF cm⁻², 1.70 mF cm⁻² and 1.27 mF cm⁻², respectively. The polarization curves normalized by ECSA (Figure S9) further confirms that the intrinsic OER activity of the IrO_x/9R-BaIrO₃ catalyst far exceeds that of IrO₂ and 6H-SrIrO₃.

In addition, the electrochemical stability of IrO_x/9R-BaIrO₃ was evaluated by long-term chronopotentiometry measurement at a constant current density of 10 mA cm⁻²_{geo}, in comparison with commercial IrO₂ and as-synthesized 6H-SrIrO₃ (Figure 2e). IrO₂ and 6H-SrIrO₃ lost their electrochemical activity after 3 h and 5 h of galvanostatic electrolysis at 10 mA cm⁻²_{geo}, respectively. Similar phenomena were also observed in previous reports.^{25, 37} Evidently, the IrO_x/9R-BaIrO₃ demonstrated good electrochemical stability during the 2 days (48 h) continuous operation, and the overpotential for IrO_x/9R-BaIrO₃ only slightly increased by 50 mV. Stability tests of these catalysts at constant potentials (Figure S10) further show that the IrO_x/9R-BaIrO₃ catalyst displays better stability than 6H-SrIrO₃ and IrO₂.

To understand the origin of the excellent OER activity of $IrO_x/9R$ -Ba IrO_3 , we further investigated $IrO_x/9R$ -Ba IrO_3 , 6H-Sr IrO_3 and IrO_2 catalysts using XPS, IrL_3 edge X-ray absorption near edge structure (XANES) spectra, ultraviolet photoelectron spectroscopy (UPS) and the temperature dependent resistivity measurements (see details in Materials and Methods). Figure 3a

compares the Ir 4f XPS spectra of IrO₂, 6H-SrIrO₃ and IrO_x/9R-BaIrO₃, which were calibrated with respect to C 1s at a binding energy of 284.5 eV. Deconvolution of the Ir XPS peaks of IrO₂ in Figure 3a reveals that the binding energies of Ir 4f_{7/2} at 62.00 eV and 4f_{5/2} at 64.95 eV, which are consistent with the reported Ir⁴⁺ XPS spectrum for IrO₂.³⁸ The Ir 4f_{7/2} XPS peak for 6H-SrIrO₃ is shifted to higher binding energy (62.15 eV) compared with IrO₂. Moreover, the Ir 4f_{7/2} XPS peak in IrO_x/9R-BaIrO₃ is further shifted to higher binding energy (62.23 eV) than 6H-SrIrO₃, indicating that the average Ir oxidation state of the surface-layer structures in IrO_x/9R-BaIrO₃ is higher than +4 and the existence of high-valence Ir (Ir⁵⁺) species³⁹⁻⁴⁰ on the surface of IrO_x/9R-BaIrO₃. Moreover, the deconvolution of Ir 4f XPS peaks for IrO_x/9R-BaIrO₃ (Figure S11) reveals additional peaks at the higher energy along with the peaks of Ir⁴⁺ species and the relative content of Ir⁵⁺ species is estimated to be ~15.1%. All of these indicate that the IrO_x nanoparticles uniformly anchored on the surface of 9R-BaIrO₃ have a higher valence beyond Ir⁴⁺.

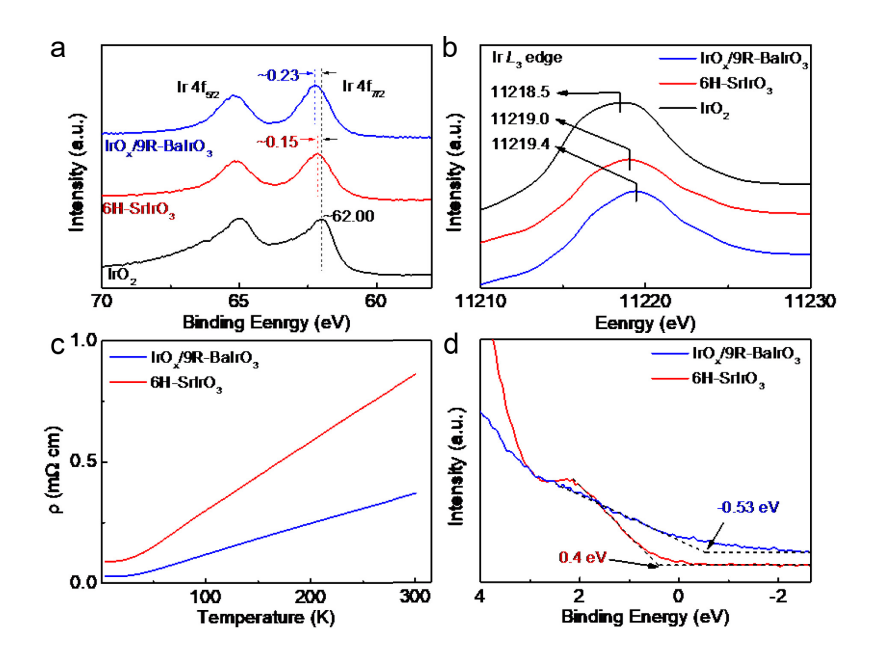


Figure 3. Characterizations of the electronic structures of various Ir-based catalysts. (a) XPS spectra of the Ir 4f peaks for IrO_x/9R-BaIrO₃, 6H-SrIrO₃ and IrO₂. (b) Ir L₃-edge XANES region of IrO_x/9R-BaIrO₃, 6H-SrIrO₃ and IrO₂. (c) Temperature dependent resistivity and (d) UPS spectra of the IrO_x/9R-BaIrO₃ and 6H-SrIrO₃ samples.

Figure 3b shows the Ir L_3 -edge XANES spectra of IrO_x/9R-BaIrO₃, 6H-SrIrO₃ and IrO₂, which are characterized by the white-line peaks. Clearly, the white-line peak position (Figure 3b) and zero-crossing point of first derivative of Ir L_3 -edge XANES spectroscopy (Figure S12a) of IrO_x/9R-BaIrO₃ shift to higher energies compared with 6H-SrIrO₃ and IrO₂, which suggests the average valence state of Ir in IrO_x/9R-BaIrO₃ is higher than that in 6H-SrIrO₃ and IrO₂ (+4).⁴¹ It is worth noting that because XANES is a bulk-sensitive analytical technique (using high-energy incident X-rays), the white line energy represents average value of the iridium atoms from both

the surface layer and the bulk. Therefore, the higher than 4+ average valence state of Ir in IrO_x/9R-BaIrO₃ suggests that the amount of amorphous IrO_x with high-valence Ir (Ir⁵⁺) species on the surface of BaIrO₃ is noticeable and detectable, which is consistent with the XPS spectra and HAADF-STEM image discussed above. It was reported that the under-coordinated disordered IrO₆ octahedrons with higher oxidation states in amorphous IrO_x can act as more electrophilic centers and enhance the OER activity¹⁸ as compared to the more ordered IrO₆ octahedrons in crystalline IrO₂. Furthermore, recent *operando* spectroscopic studies and DFT calculations show that the OER on the IrO_x surface is controlled by the formation of Ir⁵⁺ species leading to the appearance of electron-deficient oxygen species bound to single Ir atoms (μ_1 -O and μ_1 -OH) that are responsible for water activation and oxidation.³² These considerations suggest that the higher relative content of the high-valence IrO_x formed on the surface of 9R-BaIrO₃ that are derived from the face-sharing trimer of IrO₆ octahedrons could serve as the highly active layer responsible for the enhanced OER activity in iridium-based perovskite electrocatalysts.

We further performed temperature dependent resistivity and UPS measurements to study the electronic properties of IrO_x/9R-BaIrO₃ and 6H-SrIrO₃. The monotonically decreasing resistivity upon cooling (Figure 3c) indicates both IrO_x/9R-BaIrO₃ and 6H-SrIrO₃ samples exhibit intrinsic metallic behavior. Moreover, the electrical conductivity of IrO_x/9R-BIrO₃ at room temperature is twice that of 6H-SrIrO₃. The UPS spectra (Figure 3d) show both IrO_x/9R-BaIrO₃ and 6H-SrIrO₃ with significant electron distributions at the Fermi level, which agree with the intrinsic metallic conductivity. The larger density of state (DOS) at the Fermi level for IrO_x/9R-BaIrO₃ than that of 6H-SrIrO₃ explains the enhanced conductivity of IrO_x/9R-BaIrO₃. These observations are also consistent with the EIS measurements (Figure 2c) showing a smaller charge transfer resistance for IrO_x/9R-BaIrO₃. The higher electrical conductivity in IrO_x/9R-BaIrO₃ ensures faster charge transfer between catalyst-electrolyte and catalyst-support electrode interfaces, which is also beneficial for enhancing the overall catalytic performance.

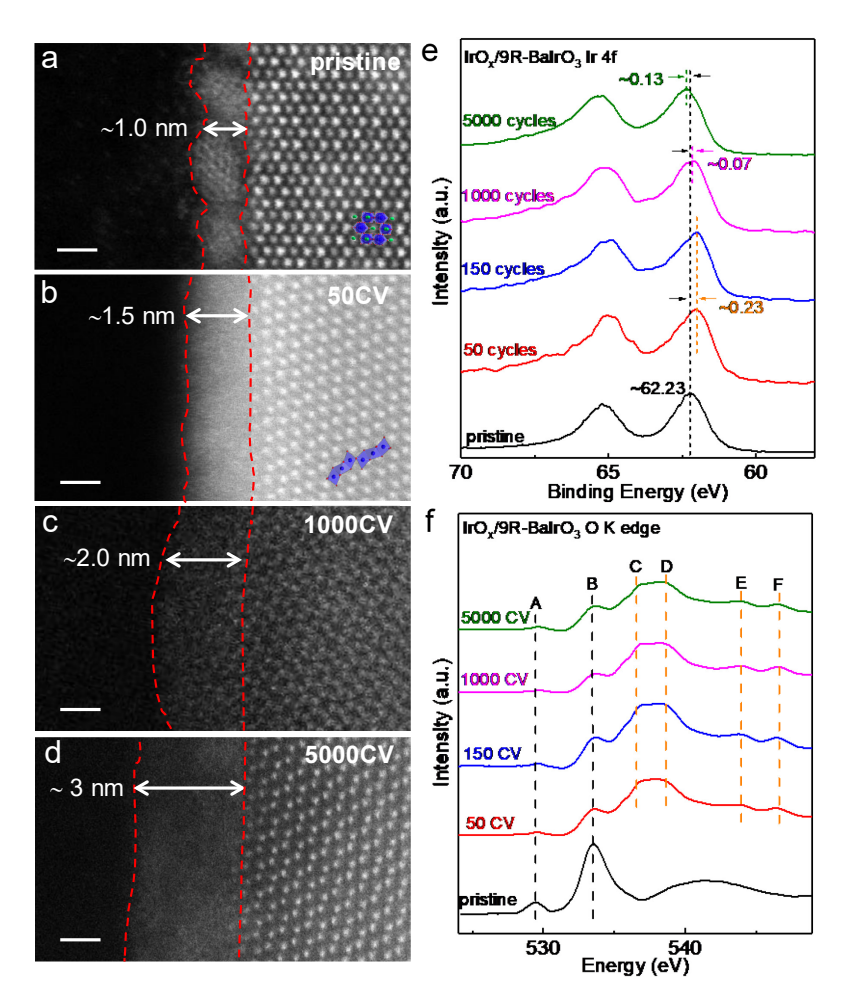


Figure 4. Evolution of the surface structure of IrO_x/9R-BaIrO₃ during acidic OER. (a-d) Lattice-resolved HAADF-STEM images of the surface of IrO_x/9R-BaIrO₃ including pristine, after 50 cycles, after 1000 cycles, and 5000 CV cycles. Scale bars, 1 nm. Simulated structures (9R-BaIrO₃ with the exposed {001} facet, two face-shared IrO₆ octahedral trimers after Ba is leached) are superimposed on part of the HAADF-STEM images. Ba, green ball; Ir, blue ball; O, red ball. (e) Ir 4f XPS spectra and (f) O K-edge XANES spectra of IrO_x/9R-BaIrO₃ including pristine, after 50, 150, 1000 and 5000 CV cycles.

To further unravel the evolution of surface structures of IrO_x/9R-BaIrO₃ during acidic OER, we employed lattice-resolved HAADF-STEM imaging, XPS and O K-edge XANES to systematically investigate the surface morphologies, surface chemical states and local atomic structures as the electrochemical reaction progressed. Figure 4a-d show HAADF-STEM images of the surface structures of the pristine IrO_x/9R-BaIrO₃, and after 50, 1000 and 5000 cyclic voltammetry (CV) cycles, respectively. After 50 cycles, the 1-nm IrO_x nanoparticles on the surface were transformed into an amorphous layer (Figure 4b). As the acidic OER continues, the thickness of the amorphous layer on the surface of 9R-BaIrO₃ grows from 1.5 nm (50 cycles) to 2.0 nm (1000 cycles) and 3.0 nm (5000 cycles). In addition, the 9R-BaIrO₃ layer (the inner layer beneath

the IrO_x nanoparticles on the right sides of Figure 4b-d) evolved into IrO₆ octahedron structures, which evolved from the initial face-sharing IrO₆ trimer of 9R-BaIrO₃ but they are much more under-coordinated disordered IrO₆ octahedrons due to the reconstruction. These changes are highlighted by the schematic crystal structures superimposed over the lattice fringe images in Figure 4a,b. This evolution is because of the further collapse of the 9R-BaIrO₃ crystal structure due to the continuous Ba leaching during acidic OER process (Figure S13). Even though the OER process of 9R-BaIrO₃ (synthesized by CSSR)²⁶ has been studied, the initial active layer and evolution of IrO_x/9R-BaIrO₃ are totally different, which led to much better acidic OER activity and stability compared with 9R-BaIrO₃.

The surface chemical states of the IrO_x/9R-BaIrO₃ catalysts after different CV cycles were inspected by XPS (Figure 4e). In the Ir 4f XPS spectrum of pristine IrO_x/9R-BaIrO₃, the peak of Ir $4f_{7/2}$ is located at ~62.23 eV. After 50 cycles, the Ir $4f_{7/2}$ peak shifted to lower binding energy at ~62.00 eV, consistent with the binding energy of Ir⁴⁺, indicating the initially formed amorphous layer contains Ir⁴⁺ species. The O K-edge XANES spectra (Figure 4f) show the Ir-O covalency and local structure of the formed amorphous layer after 50 cycles is very similar to pristine IrO_x/9R-BaIrO₃ (characteristic peak A at 529.2 eV and peak B at 533.4 eV), which means the Ir⁴⁺ amorphous layer after 50 cycles has similar Ir–O covalency and local structure of IrO_x (for example, amorphous Ir⁴⁺O_xH_y) but evidently not IrO₂. In comparison, the O K-edge XANES spectrum of the standard IrO₂ sample exhibits rather different spectral features: weaker covalent interactions of Ir-O bonds with pre-edge feature at 530.0 eV and lower energy feature for peak B at 532.2 eV (Figure S14). Such Ir⁴⁺O_xH_v amorphous layer has also been proposed in IrO₂⁴³ and SrCo_{0.9}Ir_{0.1}O_{3-δ} perovskite²⁵ during acidic OER. After 150 cycles, the amorphous layer on 9R-BaIrO₃ is still Ir⁴⁺O_xH_y based on the fact that the positions of both Ir 4f_{7/2} peak and peak A and peak B of O Kedge XANES spectrum are almost unchanged. As acidic OER continues, the Ir 4f7/2 peak goes back to high binding energy that is very close to ~62.23 eV after 1000 cycles, which suggests the Ir⁵⁺ species are formed in the 2 nm amorphous layer. The peak A and peak B of O K-edge XANES spectrum (magenta curve in Figure 4f) for the formed surface structures after 1000 cycles are at the same positions as that after 150 cycles and 50 cycles. These indicate the Ir-O covalency and local structures of formed amorphous layer (after 1000 cycles) are almost unchanged but the valence state of Ir was increased to +5, that is, Ir⁵⁺O_x amorphous layer is formed after 1000 cycles. After 5000 cycles, the thickness of the amorphous layer increased to 3 nm (Figure 4d). The Ir $4f_{7/2}$ peak upshifts to ~62.36 eV, which is even higher than that of pristine IrO_x/9R-BaIrO₃, indicating more Ir⁵⁺O_x amorphous layer is formed on the surface of 9R-BaIrO₃. Cycle-dependent polarization curves of IrO_x/9R-BaIrO₃ catalysts (Figure S15) demonstrates 1 nm IrO_x nanoparticles, Ir⁴⁺O_xH_y amorphous layer and Ir⁵⁺O_x amorphous layer exhibit high activity for acidic OER. Based on the above observations, we propose that during the evolution of surface active-layer structures on IrO_x/9R-BaIrO₃ during acidic OER, the initial IrO_x nanoparticles/9R-BaIrO₃ evolved into amorphous Ir⁴⁺O_xH_y /IrO₆ octahedrons, and then to amorphous Ir⁵⁺O_x /IrO₆ octahedrons.

Because four new peaks also emerged in the O K-edge XANES spectra for IrO_x/9R-BaIrO₃

during acidic OER, we further compared the O K-edge XANES spectra (Figure S14) and Raman spectra (Figure S16) of BaSO₄ and IrO_x/9R-BaIrO₃ after different cycles. It appears that some BaSO₄ was formed due to the Ba leaching during the acidic OER in H₂SO₄ solution and adsorbed on the 9R-BaIrO₃ surface (note that BaSO₄ is insoluble). Even though inductively coupled plasma optical emission spectroscopy (ICP-OES) measurements (Figure S13) clearly show that Ba is leaching from 9R-BaIrO₃ during acidic OER, the Ba 3d XPS spectra for the IrO_x/9R-BaIrO₃ catalysts after different CV cycles (Figure S17) exhibit similar spectral shape. This may be due to the adsorbed BaSO₄ on all samples. To assure that the observed electrochemistry is not due to BaSO₄, the electrochemical performance of IrO_x/9R-BaIrO₃ was examined in comparison with other catalysts in 1 M HClO₄ and 0.5 M H₂SO₄ (Figure S18a,b). The minor differences between the electrochemical behaviors in 1 M HClO₄ or 0.5 M H₂SO₄ do not impact the conclusions in this work. BaSO₄ has no electrochemical OER activity (Figure S18c). The evolution of ECSA (Figure S19) reveals increasing surface area over thousands of CV cycles and the intrinsic activity at the select cycles (Figure S20) indicates that the intrinsic activity decreases over time.

In contrast, the HAADF-STEM image of the 6H-SrIrO₃ catalyst after 5000 CV cycles (Figure S21) shows that there is no amorphous layer formed on the surface of 6H-SrIrO₃ during acidic OER. The different dissolution mechanisms of 9R-BaIrO₃ and 6H-SrIrO₃ may be due to the different crystal structures (Figure S22). The robust trimers of face-sharing IrO₆ octahedrons in 9R-BaIrO₃ could allow better preservation of some IrO₆ octahedrons when Ba is leached than the more weakly connected octahedrons in 6H-SrIrO₃ structure, in which the IrO₆ octahedrons are more easily dissolved when Sr is leached. The Sr 3d XPS spectra (Figure S23a) show the gradual leaching of Sr element during the acidic OER, but there was even no detectable XPS signal for Sr element on the surface of 6H-SrIrO₃ after 5000 CV cycles. The Ir 4f XPS spectrum for 6H-SrIrO₃ (Figure S23b) show that the Ir $4f_{7/2}$ peak shifted to low binding energy around ~62.00 eV after 50 cycles, which suggests the surface layer are Ir⁴⁺ species. Even after 1000 cycles, the surface layer for 6H-SrIrO₃ still showed Ir⁴⁺ species. The cycle-dependent O K-edge XANES spectra for 6H-SrIrO₃ (Figure S24) show the local structures of the surface layer (from 50 cycles to 1000 cycles) are also almost unchanged and similar to the pristine 6H-SrIrO₃ based on the similar characteristic peak A and peak B, indicating the surface active-layer structures for the 6H-SrIrO₃ catalysts are Ir⁴⁺O₆ octahedron layer. After 5000 cycles, the local structures of the surface layer on 6H-SrIrO₃ are almost unchanged but become Ir⁵⁺O₆ octahedron layers (Figure S24 and olive curve in Figure S23b). Highly sensitive O K-edge XANES spectrum (magenta curve in Figure S24) shows a little SrSO₄ adsorbed on the surface of 6H-SrIrO₃ due to Sr leaching after 5000 cycles. Chronopotentiometric measurement (red curve in Figure 2e) shows that 6H-SrIrO₃ loses electrochemical activity after 5 h of galvanostatic electrolysis. These results clearly demonstrate the surface active-layer structures for 6H-SrIrO₃ catalysts are Ir⁴⁺O₆ octahedron layers, however, the Ir⁵⁺O₆ octahedron (excessively oxidized) layers are deactivated for acidic OER. These could potentially explain the inferior OER catalytic performance of 6H-SrIrO₃ in comparison to IrO_x/9R-BaIrO₃.

Conclusion

In summary, we have synthesized IrO_x nanoparticles uniformly anchored on 9R-BaIrO₃ (IrO_x/9R-BaIrO₃) made by solution calcination followed by a strong acid treatment. The IrO_x/9R-BaIrO₃ shows the highest iridium mass activity among the reported iridium-based perovskite electrocatalysts for the acidic OER to date, and displays good electrochemical stability. By combining lattice-resolved STEM imaging, surface-sensitive XANES and XPS analyses, we systematically studied the surface active-layer structure evolution in IrO_x/9R-BaIrO₃ and showed that the initial IrO_x nanoparticles/9R-BaIrO₃ evolve into amorphous Ir⁴⁺O_xH_y/IrO₆ octahedrons and then to amorphous Ir⁵⁺O_x/IrO₆ octahedrons during acidic OER. The higher content of the amorphous high valence Ir⁵⁺O_x species evolved from the 1-nm IrO_x particles and the enhanced metallic conductivity of IrO_x/9R-BaIrO₃ are responsible for the enhanced acidic OER activity of IrO_x/9R-BaIrO₃ over that of related iridium perovskite catalyst 6H-SrIrO₃ and IrO₂. This work not only demonstrates a highly active OER catalysts in acidic solution, but also provides in-depth understanding of the surface active-layer structure evolution in perovskite electrocatalysts and a new approach for engineering superb acidic OER catalysts.

Materials and Methods

Synthesis of IrO_x/9R-BaIrO₃ and 6H-SrIrO₃

K₂IrCl₆ (99.99%) was purchased from Aladdin. Sr(NO₃)₂, Ba(NO₃)₂, citric acid monohydrate (C₆H₈O₇·H₂O), ethylene glycol, HCl, H₂SO₄ and ethanol were purchased from Shanghai Research Institute of Chemical Industry. 5% Nafion (99.9%) and IrO₂ (99.9%) were purchased from Sigma-Aldrich. All chemical reagents were used as received without further purification. All aqueous solutions were prepared using deionized water with a resistivity of 18.2 M Ω cm⁻¹. In a typical synthesis process, 350 mg of Ba(NO₃)₂ and 280 mg of C₆H₈O₇·H₂O with the molar ratio of 1:1 were mixed with 5 mL deionized water to form the solution-1, and K₂IrCl₆ (80 mg) was dissolved into 4 mL ethylene glycol to form the solution-2. Then, the solution-1 was added dropwise to the solution-2 under vigorous stirring and the resulting mixture was dried at 150 °C overnight to obtain a brown solid product as the precursor. Then, the precursor was transferred to a crucible and heated in air at 200 °C (6 h), 300 °C (6 h), 500 °C (3 h), and 700 °C (6 h). The heating rate was 1.7 °C min⁻¹. The addition of organic citric acid results in more heat released at elevated temperature, which was thought to favor the generation of high-valent iridium species. But carbonate can be formed, which leads to the formation of BaCO₃ impurity phase. The obtained solid product was treated with 10 ml of 1 M HCl for 6 h to remove the BaCO₃ impurity and to yield the targeted catalyst material.

For the synthesis of 6H-SrIrO₃, the experimental procedures were almost the same as those for the synthesis of IrO_x/9R-BaIrO₃, except that Ba(NO₃)₂ was replaced by Sr(NO₃)₂ (280 mg).

Structure characterization

The powder X-ray diffraction (XRD) patterns were collected on a Philips X'pert Pro Super

diffractometer with Cu K_{α} radiation ($\lambda = 1.5418$ Å). The scanning electron microscopy (SEM) images were obtained on a JSM-6700F scanning electron microscope operating at 5 kV. Transmission electron microscopy (TEM), high resolution TEM (HRTEM) and energy dispersive X-ray (EDX) spectral analysis were performed on a JEM-2100F microscope operating at an acceleration voltage of 200 kV. Sub-Å-resolution aberration-corrected high-angle annular dark field scanning transmission electron microscopy (HAADF-STEM) imaging and the corresponding EDX spectroscopy were conducted on a JEM-ARM 200F TEM at the accelerating voltage of 200 kV. The temperature dependent resistivity measurement was performed on pressed powder pellet (~6 mm × 6 mm × 0.5 mm) by a four-point probe resistance measurement using a Quantum Design Physical Property Measurement System (PPMS). The various sample powders (IrO₂, 6H-SrIrO₃ and IrO_x/9R-BaIrO₃) were pressed into a cuboid pellet (~6 mm × 6 mm × 0.5 mm), which were annealed at 500 °C (2 h) in air to eliminate the effect of particle contact geometry. XPS and UPS were acquired at the BL10B beamline in the National Synchrotron Radiation Laboratory (NSRL), China. The XPS spectra were recorded with Al Ka (1486.6 eV) as the excitation source and the resolution of electron energy analyzer (Scienta R3000) is ~0.02 eV. The binding energies obtained in the XPS spectral analysis were corrected for specimen charging by referencing C 1s to 284.5 eV. The Fermi level E_F is located at E=0 which was measured from the Fermi edge of an evaporated Au film. The sample was biased by -10.0 V in order to acquire distinct the secondary-electron cutoff of the spectrum and valence band spectrum chosen for 170 eV of synchrotron radiation light excitation energy. The Ir L₃-edge XAFS data were collected at 1W1B station in Beijing Synchrotron Radiation Facility (BSRF) and BL14W1 beamline of the Shanghai Synchrotron Radiation Facility (SSRF), China. The storage ring of BSRF and SSRF were operated at 2.5 and 3.5 GeV with a maximum current of 250 mA, respectively. The O K-edge X-ray absorption nearedge (XANES) spectra were performed at the Beamlines MCD-A and MCD-B (Soochow Beamline for Energy Materials) in NSRL, which were measured in the total electron yield mode in a vacuum chamber ($<5 \times 10^{-8}$ Pa).

Electrochemical measurements

All the electrochemical measurements were performed with a three-electrode system on a CHI760E instrument (Chenhua, China). A graphite rod and an Ag/AgCl electrode (saturated KCl solution) were used as the counter electrode and reference electrode, respectively. Typically, 4 mg of catalysts were dispersed in 1 ml mixture solution of 4:1 v/v of water/ ethanol. Then, 30 μL Nafion solution (Sigma Aldrich, 5 wt %) was added and subsequently sonicated to form a homogeneous ink. 5 μL of the dispersion was loaded onto a glassy carbon electrode (GCE) of 3 mm in diameter. The polarization curves were measured in O₂-saturated 0.5 M H₂SO₄ solution with a scan rate of 5 mV s⁻¹. The data were iR-corrected. Electrochemical impedance spectroscopy measurements were made by applying an AC voltage with 5 mV amplitude in a frequency range from 100 KHz to 100 mHz at overpotential of 300 mV, respectively. Carbon paper (1×1 cm²) was used as the catalyst support for chronopotentiometric measurement. Mass loading on carbon paper electrode is the same as that on GCE (0.283 mg cm⁻²).

Electrochemically active surface area (ECSA) and mass activity calculations

The ECSA for each catalyst was estimated from the electrochemical double-layer capacitance (C_{dl}), which is expected to be linearly proportional to the ECSA. The C_{dl} was determined by measuring the non-Faradic capacitive current associated with double-layer charging from the scan rate dependence of CV. The current response was taking in the potential window (0.585–0.685 V vs. RHE) for the CV with different scan rates (*v*: 40–200 mV s⁻¹). Moreover, the double-layer charging current (i_c) is equal to the product of the scan rate (v) and the C_{dl}, as given by equation (1):

$$i_c = \nu C_{dl} \tag{1}$$

Thus, a plot of i_c as a function of v obtains a straight line with a slope equal to C_{dl}. The ECSA of the samples is calculated from the C_{dl} according to equation (2):

$$EASA = C_{dl} / C_s$$
 (2)

where C_s is the specific capacitance of the catalyst. The general specific capacitances of $C_s = 0.035$ mF cm⁻² was used based on typical reported values.¹⁵

The mass activity (A g^{-1}) values of the catalysts were calculated from the loading mass of iridium (*m*) and the corresponding current (*i*) at 1.5 V vs. RHE:

Mass activity =
$$i / m$$
 (3)

With the catalyst loading mass of 0.02 mg under 1.5 V vs. RHE, the current density for $IrO_x/9R$ -Ba IrO_3 is ~26.2 mA cm⁻² (range from 26.2 to 27.4 mA cm⁻²). We considered the effect of leached Ba (IrO_x layer) when calculating the iridium mass activity of $IrO_x/9R$ -Ba IrO_3 following the approximate method. The iridium mass activity we reported is the average value that is estimated as $168 \text{ A g}_{Ir}^{-1}$.

Supporting Information

Additional structural characterizations of the various catalysts, additional electrochemical measurements of the various catalysts, the first and second derivatives of Ir L_3 -edge XANES spectra, Raman spectra and additional XPS for IrO_x/9R-BaIrO₃ after different cycles, XPS spectra and O K-edge XANES for 6H-SrIrO₃ after different cycles, and the detailed discussion. The Supporting Information is available free of charge on the ACS Publications website.

Acknowledgements

This work was financially supported by the National Natural Science Foundation of China (Grants No. 11975234, 11775225, 12075243 and 12005227), Users with excellence program of Hefei science center CAS, (No. 2019HSC-UE002, 2020HSC-UE002, 2020HSC-CIP013). H. S. and S. J. thank the support of US NSF CHE-1955074. The authors would like to thank BSRF, SSRF and NSRL for the synchrotron beamtime. This work was partially carried out at the USTC Center for Micro and Nanoscale Research and Fabrication.

Notes

The authors declare no competing financial interests.

References

- 1. Seh, Z. W.; Kibsgaard, J.; Dickens, C. F.; Chorkendorff, I.; Nørskov, J. K.; Jaramillo, T. F., Combining theory and experiment in electrocatalysis: Insights into materials design. *Science* **2017**, *355*, eaad4998.
- 2. Montoya, J. H.; Seitz, L. C.; Chakthranont, P.; Vojvodic, A.; Jaramillo, T. F.; Nørskov, J. K., Materials for solar fuels and chemicals. *Nature materials* **2017**, *16* (1), 70-81.
- 3. Reier, T.; Nong, H. N.; Teschner, D.; Schlögl, R.; Strasser, P., Electrocatalytic oxygen evolution reaction in acidic environments—reaction mechanisms and catalysts. *Advanced Energy Materials* **2017**, *7* (1), 1601275.
- 4. Suntivich, J.; May, K. J.; Gasteiger, H. A.; Goodenough, J. B.; Shao-Horn, Y., A perovskite oxide optimized for oxygen evolution catalysis from molecular orbital principles. *Science* **2011**, *334* (6061), 1383-1385.
- 5. Trotochaud, L.; Young, S. L.; Ranney, J. K.; Boettcher, S. W., Nickel-iron oxyhydroxide oxygen-evolution electrocatalysts: the role of intentional and incidental iron incorporation. *Journal of the American Chemical Society* **2014**, *136* (18), 6744-6753.
- 6. Song, F.; Hu, X., Exfoliation of layered double hydroxides for enhanced oxygen evolution catalysis. *Nature communications* **2014**, *5*, 4477.
- 7. Burke, M. S.; Enman, L. J.; Batchellor, A. S.; Zou, S.; Boettcher, S. W., Oxygen Evolution Reaction Electrocatalysis on Transition Metal Oxides and (Oxy)hydroxides: Activity Trends and Design Principles. *Chemistry of Materials* **2015**, *27* (22), 7549-7558.
- 8. Zhang, B.; Zheng, X.; Voznyy, O.; Comin, R.; Bajdich, M.; García-Melchor, M.; Han, L.; Xu, J.; Liu, M.; Zheng, L., Homogeneously dispersed multimetal oxygen-evolving catalysts. *Science* **2016**, *352* (6283), 333-337.
- 9. Suen, N.-T.; Hung, S.-F.; Quan, Q.; Zhang, N.; Xu, Y.-J.; Chen, H. M., Electrocatalysis for the oxygen evolution reaction: recent development and future perspectives. *Chemical Society Reviews* **2017**, *46* (2), 337-365.
- 10. Huang, Z.-F.; Song, J.; Du, Y.; Xi, S.; Dou, S.; Nsanzimana, J. M. V.; Wang, C.; Xu, Z. J.; Wang, X., Chemical and structural origin of lattice oxygen oxidation in Co–Zn oxyhydroxide oxygen evolution electrocatalysts. *Nature Energy* **2019**, *4* (4), 329-338.
- 11. Yang, Y.; Dang, L.; Shearer, M. J.; Sheng, H.; Li, W.; Chen, J.; Xiao, P.; Zhang, Y.; Hamers, R. J.; Jin, S., Highly active trimetallic NiFeCr layered double hydroxide electrocatalysts for oxygen evolution reaction. *Advanced Energy Materials* **2018**, *8* (15), 1703189.
- 12. Carmo, M.; Fritz, D. L.; Mergel, J.; Stolten, D., A comprehensive review on PEM water electrolysis. *International journal of hydrogen energy* **2013**, *38* (12), 4901-4934.
- 13. Kibsgaard, J.; Chorkendorff, I., Considerations for the scaling-up of water splitting catalysts.

- *Nature Energy* **2019**, *4* (6), 430.
- 14. Lee, Y.; Suntivich, J.; May, K. J.; Perry, E. E.; Shao-Horn, Y., Synthesis and activities of rutile IrO₂ and RuO₂ nanoparticles for oxygen evolution in acid and alkaline solutions. *The journal of physical chemistry letters* **2012**, *3* (3), 399-404.
- 15. McCrory, C. C.; Jung, S.; Peters, J. C.; Jaramillo, T. F., Benchmarking heterogeneous electrocatalysts for the oxygen evolution reaction. *Journal of the American Chemical Society* **2013**, *135* (45), 16977-16987.
- 16. Nong, H. N.; Oh, H. S.; Reier, T.; Willinger, E.; Willinger, M. G.; Petkov, V.; Teschner, D.; Strasser, P., Oxide-Supported IrNiO_x Core–Shell Particles as Efficient, Cost-Effective, and Stable Catalysts for Electrochemical Water Splitting. *Angewandte Chemie International Edition* **2015**, *54* (10), 2975-2979.
- 17. Reier, T.; Pawolek, Z.; Cherevko, S.; Bruns, M.; Jones, T.; Teschner, D.; Selve, S. r.; Bergmann, A.; Nong, H. N.; Schlögl, R., Molecular insight in structure and activity of highly efficient, low-Ir Ir–Ni oxide catalysts for electrochemical water splitting (OER). *Journal of the American Chemical Society* **2015**, *137* (40), 13031-13040.
- 18. Gao, J.; Xu, C.-Q.; Hung, S.-F.; Liu, W.; Cai, W.; Zeng, Z.; Jia, C.; Chen, H. M.; Xiao, H.; Li, J., Breaking long-range order in iridium oxide by alkali ion for efficient water oxidation. *Journal of the American Chemical Society* **2019**, *141* (7), 3014-3023.
- 19. Nong, H. N.; Reier, T.; Oh, H.-S.; Gliech, M.; Paciok, P.; Vu, T. H. T.; Teschner, D.; Heggen, M.; Petkov, V.; Schlögl, R., A unique oxygen ligand environment facilitates water oxidation in hole-doped IrNiO_x core–shell electrocatalysts. *Nature Catalysis* **2018**, *I* (11), 841-851.
- 20. Spoeri, C.; Kwan, J. T. H.; Bonakdarpour, A.; Wilkinson, D. P.; Strasser, P., The stability challenges of oxygen evolving catalysts: towards a common fundamental understanding and mitigation of catalyst degradation. *Angewandte Chemie International Edition* **2017**, *56* (22), 5994-6021.
- 21. Song, J.; Wei, C.; Huang, Z.-F.; Liu, C.; Zeng, L.; Wang, X.; Xu, Z. J., A review on fundamentals for designing oxygen evolution electrocatalysts. *Chemical Society Reviews* **2020**, *49* (7), 2196-2214.
- 22. Huang, J.; Sheng, H.; Ross, R. D.; Han, J.; Wang, X.; Song, B.; Jin, S., Modifying redox properties and local bonding of Co₃O₄ by CeO₂ enhances oxygen evolution catalysis in acid. *Nature Communications* **2021**, *12*, 3036.
- 23. Seitz, L. C.; Dickens, C. F.; Nishio, K.; Hikita, Y.; Montoya, J.; Doyle, A.; Kirk, C.; Vojvodic, A.; Hwang, H. Y.; Norskov, J. K., A highly active and stable IrO_x/SrIrO₃ catalyst for the oxygen evolution reaction. *Science* **2016**, *353* (6303), 1011-1014.
- 24. Yang, L.; Yu, G.; Ai, X.; Yan, W.; Duan, H.; Chen, W.; Li, X.; Wang, T.; Zhang, C.; Huang, X., Efficient oxygen evolution electrocatalysis in acid by a perovskite with face-sharing IrO₆ octahedral dimers. *Nature communications* **2018**, *9*, 5236.
- 25. Chen, Y.; Li, H.; Wang, J.; Du, Y.; Xi, S.; Sun, Y.; Sherburne, M.; Ager, J. W.; Fisher, A. C.; Xu, Z. J., Exceptionally active iridium evolved from a pseudo-cubic perovskite for oxygen evolution in acid. *Nature communications* **2019**, *10*, 572.
- 26. Song, C. W.; Suh, H.; Bak, J.; Bae, H. B.; Chung, S.-Y., Dissolution-Induced Surface

- Roughening and Oxygen Evolution Electrocatalysis of Alkaline-Earth Iridates in Acid. *Chem* **2019**, *5* (12), 3243-3259.
- 27. Diaz-Morales, O.; Raaijman, S.; Kortlever, R.; Kooyman, P. J.; Wezendonk, T.; Gascon, J.; Fu, W.; Koper, M. T., Iridium-based double perovskites for efficient water oxidation in acid media. *Nature communications* **2016**, *7*, 12363.
- 28. Wan, G.; Freeland, J. W.; Kloppenburg, J.; Petretto, G.; Nelson, J. N.; Kuo, D.-Y.; Sun, C.-J.; Wen, J.; Diulus, J. T.; Herman, G. S., Amorphization mechanism of SrIrO₃ electrocatalyst: How oxygen redox initiates ionic diffusion and structural reorganization. *Science Advances* **2021**, *7* (2), eabc7323.
- 29. Danilovic, N.; Subbaraman, R.; Chang, K.-C.; Chang, S. H.; Kang, Y. J.; Snyder, J.; Paulikas, A. P.; Strmcnik, D.; Kim, Y.-T.; Myers, D., Activity–stability trends for the oxygen evolution reaction on monometallic oxides in acidic environments. *The journal of physical chemistry letters* **2014**, *5* (14), 2474-2478.
- 30. Cheng, J.-G.; Alonso, J. A.; Suard, E.; Zhou, J.-S.; Goodenough, J. B., A new perovskite polytype in the high-pressure sequence of BaIrO₃. *Journal of the American Chemical Society* **2009**, *131* (21), 7461-7469.
- 31. Flores, R. A.; Paolucci, C.; Winther, K. T.; Jain, A.; Torres, J. A. G.; Aykol, M.; Montoya, J.; Nørskov, J. K.; Bajdich, M.; Bligaard, T., Active Learning Accelerated Discovery of Stable Iridium Oxide Polymorphs for the Oxygen Evolution Reaction. *Chemistry of Materials* **2020**, *32* (13), 5854-5863.
- 32. Velasco-Vélez, J.-J.; Carbonio, E. A.; Chuang, C.-H.; Hsu, C.-J.; Lee, J.-F.; Arrigo, R.; Hävecker, M.; Wang, R.; Plodinec, M.; Wang, F. R.; Centeno, A.; Zurutuza, A.; Falling, L. J.; Mom, R. V.; Hofmann, S.; Schlögl, R.; Knop-Gericke, A.; Jones, T. E., Surface Electron-Hole Rich Species Active in the Electrocatalytic Water Oxidation. *Journal of the American Chemical Society* **2021**, https://doi.org/10.1021/jacs.1c01655.
- 33. McCrory, C. C.; Jung, S.; Ferrer, I. M.; Chatman, S. M.; Peters, J. C.; Jaramillo, T. F., Benchmarking hydrogen evolving reaction and oxygen evolving reaction electrocatalysts for solar water splitting devices. *Journal of the American Chemical Society* **2015**, *137* (13), 4347-4357.
- 34. Wu, Y.; Sun, W.; Zhou, Z.; Zaman, W. Q.; Tariq, M.; Cao, L.; Yang, J., Highly efficient oxygen evolution activity of Ca₂IrO₄ in an acidic environment due to its crystal configuration. *ACS omega* **2018**, *3* (3), 2902-2908.
- 35. Grimaud, A.; Demortière, A.; Saubanère, M.; Dachraoui, W.; Duchamp, M.; Doublet, M.-L.; Tarascon, J.-M., Activation of surface oxygen sites on an iridium-based model catalyst for the oxygen evolution reaction. *Nature Energy* **2016**, *2*, 16189.
- 36. Strickler, A. L.; Higgins, D.; Jaramillo, T. F., Crystalline Strontium Iridate Particle Catalysts for Enhanced Oxygen Evolution in Acid. *ACS Applied Energy Materials* **2019**, *2* (8), 5490-5498.
- 37. Beni, G.; Schiavone, L.; Shay, J.; Dautremont-Smith, W.; Schneider, B., Electrocatalytic oxygen evolution on reactively sputtered electrochromic iridium oxide films. *Nature* **1979**, *282*, 281-283.
- 38. Freakley, S. J.; Ruiz-Esquius, J.; Morgan, D. J., The X-ray photoelectron spectra of Ir, IrO₂ and IrCl₃ revisited. *Surface and Interface Analysis* **2017**, *49* (8), 794-799.

- 39. Augustynski, J.; Koudelka, M.; Sanchez, J.; Conway, B., ESCA study of the state of iridium and oxygen in electrochemically and thermally formed iridium oxide films. *Journal of electroanalytical chemistry and interfacial electrochemistry* **1984**, *160* (1-2), 233-248.
- 40. Sanchez Casalongue, H. G.; Ng, M. L.; Kaya, S.; Friebel, D.; Ogasawara, H.; Nilsson, A., In situ observation of surface species on iridium oxide nanoparticles during the oxygen evolution reaction. *Angewandte Chemie* **2014**, *126* (28), 7297-7300.
- 41. Choy, J.-H.; Kim, D.-K.; Demazeau, G.; Jung, D.-Y., L_{III}-edge XANES study on unusually high valent iridium in a perovskite lattice. *The Journal of Physical Chemistry* **1994**, *98* (25), 6258-6262.
- 42. Xu, K.; Chen, P.; Li, X.; Tong, Y.; Ding, H.; Wu, X.; Chu, W.; Peng, Z.; Wu, C.; Xie, Y., Metallic nickel nitride nanosheets realizing enhanced electrochemical water oxidation. *Journal of the American Chemical Society* **2015**, *137* (12), 4119-4125.
- 43. Kötz, R.; Neff, H.; Stucki, S., Anodic Iridium Oxide Films: XPS-Studies of Oxidation State Changes and O₂ evolution. *Journal of the Electrochemical Society* **1984**, *131* (1), 72.

TOC Graph

